THE MEASUREMENTS OF THE ROTATIONAL RAMAN CROSS SECTION OF N2 AND O2 AT 10.6 MICRONS

Morton Camac, et al

Aerodyne Research, Incorporated

Prepared for:

Office of Naval Research
Defense Advanced Research Projects Agency

February 1973

aerodyne research

THE MEASUREMENT OF THE ROTATIONAL RAMAN CROSS SECTION OF N_2 AND O_2 AT 10.6 MICRONS

Morton Camac
Principal Investigator

Robert C. Sepucha
Principal Scientist

SEMIANNUAL REPORT

February 1973

Contract No. N00014-73-C-0025
DARPA Order No. 1806
Program Code No. 2E90

Scientific Officer
Director, Physical Programs
Physical Sciences Division
Office of Naval Research
Arlington, Virginia 22217

Sponsored by
Defense Advanced Research Projects Agency
Physical Sciences Division
Arlington, Virginia 22217

Prepared for

OFFICE OF NAVAL RESEARCH
Department of the Navy
Arlington, Virginia 22217

UNCLASSIFIED
Security Classification

DOCUMENT CONTROL DATA - R & D

(Security classification of title, body of abstract and indexing annotation must be entered when the overall report is classified)

1. ORIGINATING ACTIVITY (Corporate author)	2a. REPORT SECURITY CLASSIFICATION
AERODYNE RESEARCH, INC. Tech/Ops Building Northwest Industrial Park, Burlington, Mass. 01803	Unclassified 2b. GROUP NA

3. REPORT TITLE

THE MEASUREMENT OF THE ROTATIONAL RAMAN CROSS SECTION OF N_2 AND O_2 AT 10.6 MICRONS

4. DESCRIPTIVE NOTES (Type of report and inclusive dates)

Semiannual Report

5. AUTHOR(S) (First name, middle initial, last name)

Morton Camac
Robert C. Sepucha

6. REPORT DATE	7a. TOTAL NO. OF PAGES	7b. NO. OF REFS
February 1973	58	4

8a. CONTRACT OR GRANT NO.	9a. ORIGINATOR'S REPORT NUMBER(S)
N00014-73-C-0025 b. PROJECT NO. DARPA Order No. 1806 c. Program Code No. 2E90 d.	ARI-RR22 9b. OTHER REPORT NO(S) (Any other numbers that may be assigned this report)

10. DISTRIBUTION STATEMENT

44, 2, ii of General Provisions - B-October 1969

11. SUPPLEMENTARY NOTES	12. SPONSORING MILITARY ACTIVITY
Prepared for Office of Naval Research Department of the Navy Details of illustrations in this document may be better studied on microfiche.	Defense Advanced Research Projects Agency Physical Sciences Division Arlington, Virginia 22217

13. ABSTRACT

An experimental facility was constructed to measure the rotational Raman scattering cross sections of N_2 and O_2 at 10.6 microns. The system was designed to measure the Raman cross sections relative to the CO_2 radiative absorption cross section in the 10.4-micron band. Static and dynamic calibrations of the system were devised to determine the importance of scattering from walls and dust relative to the Rayleigh and Raman components of the radiation scattered from the gas.

DD FORM 1 NOV 68 1473 REPLACES DD FORM 1473, 1 JAN 64, WHICH IS OBSOLETE FOR ARMY USE.

II-a

UNCLASSIFIED
Security Classification

14. KEY WORDS	LINK A		LINK B		LINK C	
	ROLE	WT	ROLE	WT	ROLE	WT
Rotational Raman Scattering Infrared Laser Radiation Radiative Emission From CO_2						

THE MEASUREMENT OF THE ROTATIONAL RAMAN CROSS SECTION OF N_2 AND O_2 AT 10.6 MICRONS

Morton Camac
Principal Investigator

Robert C. Sepucha
Principal Scientist

AERODYNE RESEARCH, INC.
Burlington, Massachusetts 01803

SEMIANNUAL REPORT

February 1973

Contract No. N00014-73-C-0025
DARPA Order No. 1806
Program Code No. 2E90

Effective Date:	11 July 1973
Expiration Date:	11 April 1973
Amount of Contract:	$69,015

Sponsored by

DEFENSE ADVANCED RESEARCH PROJECTS AGENCY
PHYSICAL SCIENCES DIVISION
Arlington, Virginia 22217

Prepared for

OFFICE OF NAVAL RESEARCH
DEPARTMENT OF THE NAVY
Arlington, Virginia 22217

I

TABLE OF CONTENTS

LIST OF ILLUSTRATIONS

SUMMARY

The propagation of high-intensity laser beams at 10.6 microns through the atmosphere is limited by the presence of nonlinear effects which may, under proper conditions, severely degrade the quality of, or attenuate, the laser beam. Of primary concern is stimulated Raman scattering produced by the major atmospheric constituents N_2 and O_2. To date, theoretical estimates of the Raman-scattering cross sections have been obtained by extrapolating the values measured in the visible region to 10.6 microns. No Raman-scattering cross sections have been measured at 10.6 microns, or in fact, at any wavelength above 1.0 micron. Thus, experimental verification of the wavelength dependence of the scattering cross sections over large wavelength ranges have not been possible.

This semiannual report describes Aerodyne Research's experimental program for measuring the Raman-scattering cross sections of N_2 and O_2 at 10.6 microns. By measuring the intensity of radiation scattered from a 10.6-micron laser beam by N_2 and O_2 relative to the well-known radiative emission from CO_2, only relative measurements are made. Thus, an absolute calibration is avoided, as are the numerous difficulties that arise in absolute cross-section measurements.

Besides describing the equipment fabricated for the experiment, the results of static and dynamic calibrations performed with the apparatus are reported. The static calibration uses a known blackbody source and provides a measure of the sensitivity of the detection system to radiation in the vicinity of 10 microns. The dynamic calibration is essentially a measurement of the emission from the 9.4- and 10.4-micron bands of CO_2 following laser absorption.

The calibration results indicate that the sensitivity of the experimental facility, after some modification, is more than adequate to measure the N_2 Raman-scattered intensity from a 10-joule, 10.6-micron laser beam.

The dynamic calibration of the detection system has demonstrated a sufficiently fast risetime to monitor radiation during the 0.2-microsecond laser pulse. In addition, preliminary data from the CO_2 emission yields a collisional deactivation rate constant for the excited state of CO_2 that is in good agreement with published results.

The problem associated with Raman cross-section measurements has always been the intensity of radiation scattered from walls and dust, as well as the intensity of the Rayleigh component of the scattered radiation from the gas. The preliminary data in this report indicate that radiation from the walls has been reduced to an acceptable level in the present apparatus by incorporating only a moderate amount of baffling in the optical system. Besides, the effects of dust at 10.6 microns have been found to be negligible. The last source of background radiation, Rayleigh scattering, will be eliminated by a CO_2 absorption filter in the detection system. This filter, unique for 10.6-micron laser radiation, is being designed and integrated into the experimental apparatus.

At present, the scattering chamber in the system is being enlarged, and the baffle system is being perfected to eliminate completely wall scattering. When this work is completed and the scattering cell is aligned in an intracavity mode, the Rayleigh scattering from N_2 and O_2 will be measured. Immediately afterwards, the CO_2 absorption filter will be installed in the detection system, and the Raman scattering from N_2 and O_2 will be measured.

1. INTRODUCTION

This semiannual report for DARPA/ONR covers efforts to date to determine the Raman scattering cross section for N_2 and O_2 at 10.6-microns. The experimental approach used is the measurement of the intensity of radiation scattered from a 10.6-micron laser beam by N_2 and O_2 relative to the emission from CO_2. Because the CO_2 emission is due to the transitions, $CO_2(00^O1) \rightarrow CO_2(10^O0) + h\nu$ and $_2(00^O1) \rightarrow CO_2(02^O0) + h\nu$, which have well known radiative lifetimes, only relative measurements of the Raman scattering cross sections are made. An absolute calibration is avoided as are the numerous difficulties which usually arise in an absolute cross-section measurement. The principal spectroscopic tool used for the experiment is a selective absorber composed of heated CO_2 gas, which filters the Rayleigh, dust, and wall radiation at the laser wavelength from the signal incident on the infrared detector.

2. THECRY OF THE EXPERIMENT

The rotational Raman spectrum from nitrogen produced by 10.6-micron radiation at 77°K is presented in Fig. 1. The line spacings are on the order of eight reciprocal centimeters. Peak separation from the 10.6-micron line is approximately 40 reciprocal centimeters. Isolation of the Raman radiation from the primary beam and from both the Rayleigh and wall scattering is a major concern when performing the experiment. The width of the Raman line depends on pressure and is given by

$$\Delta\nu = \frac{1}{20} p \sqrt{273^{\circ}K/T} \ \text{cm}^{-1} \quad , \qquad (1)$$

where $\Delta\nu$ is the line width due to collisional broadening, p is the pressure in atmospheres, and T is the temperature. At 100 atmospheres pressure, the line width is approximately equal to the Raman-line spacing. Below 30 atmospheres pressure, the overlap of the lines is small. However, the line overlap and line shape are not critical in this experiment, s the total scattered radiation in a band would be measured. A more serious problem at high pressures is collisional deactivation. Operation must take place over a range of pressures (1 to 10 atmospheres) to ensure that deactivation is not limiting the measurements.

Figures 2 and 3 show the experimental arrangement of the apparatus. A CO_2 10.6-micron laser pulsed once per second, illuminates nitrogen (or oxygen) gas in a scattering chamber. In Fig. 2A, the scattering chamber is outside the laser cavity, and the laser beam passes through the long vacuum cell containing the scattering region. The external power of the LUMONICS laser system is

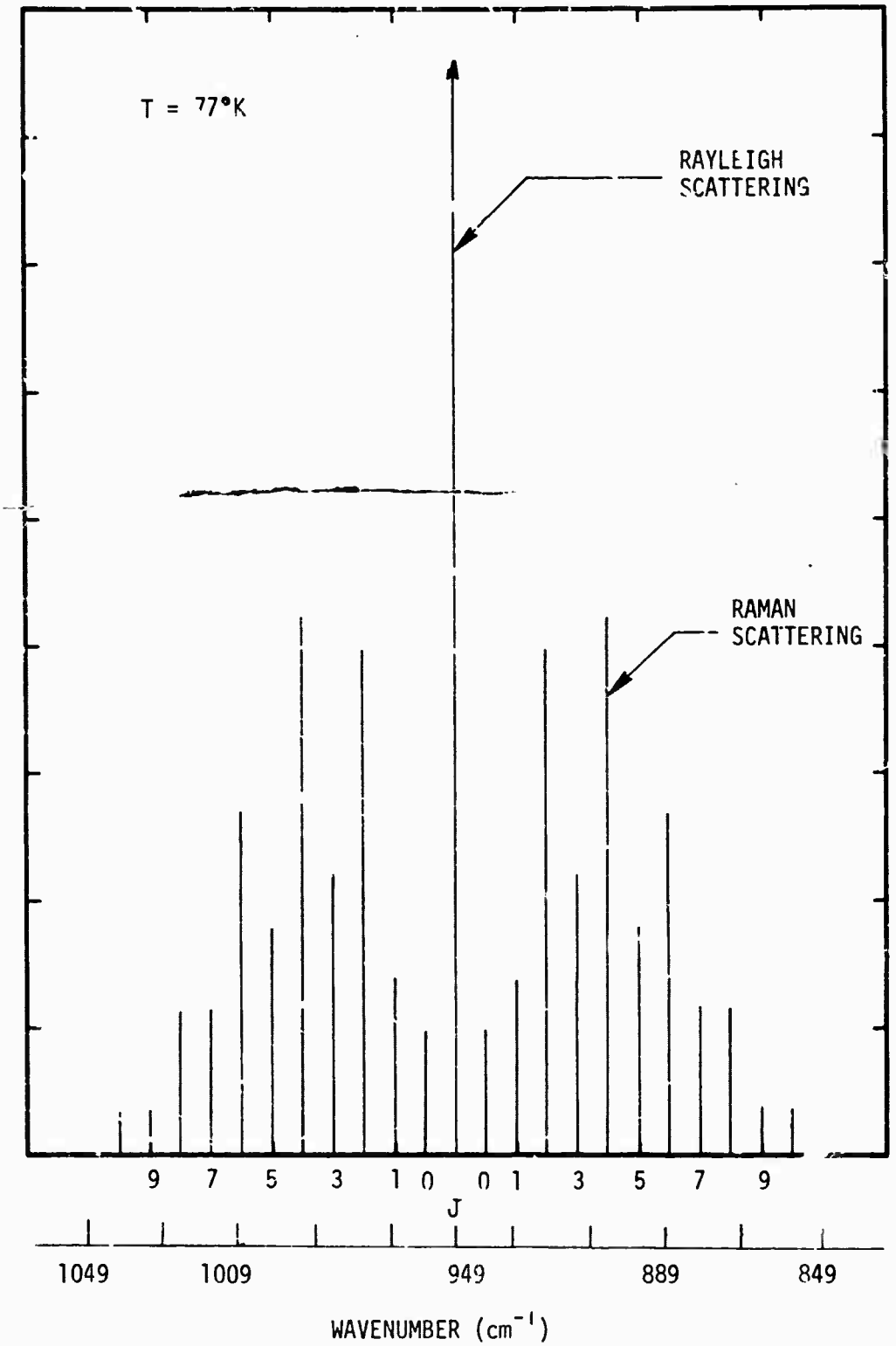

Fig. 1. Rotation Raman Spectrum of Nitrogen at 10.6μ.

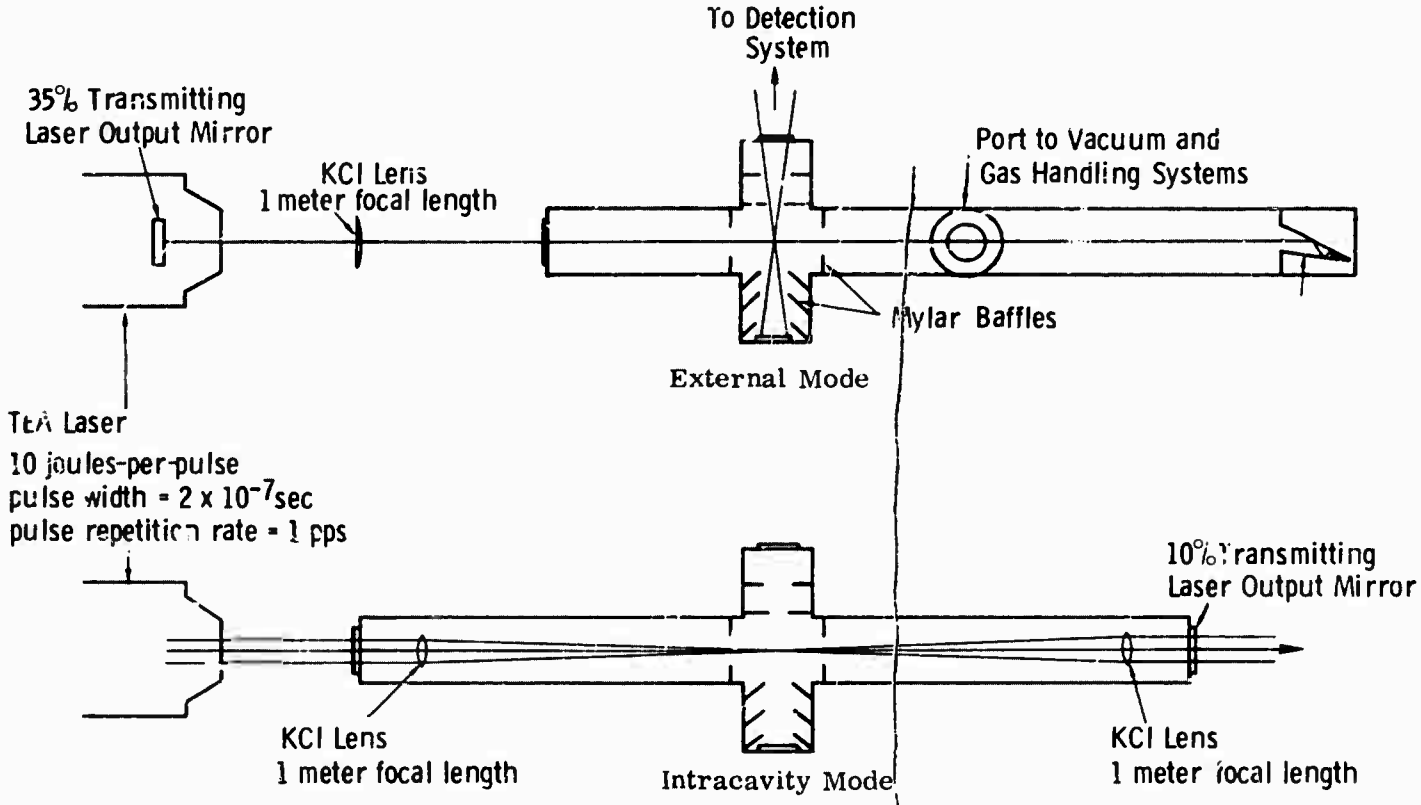

Fig. 2. Experimental Arrangement.

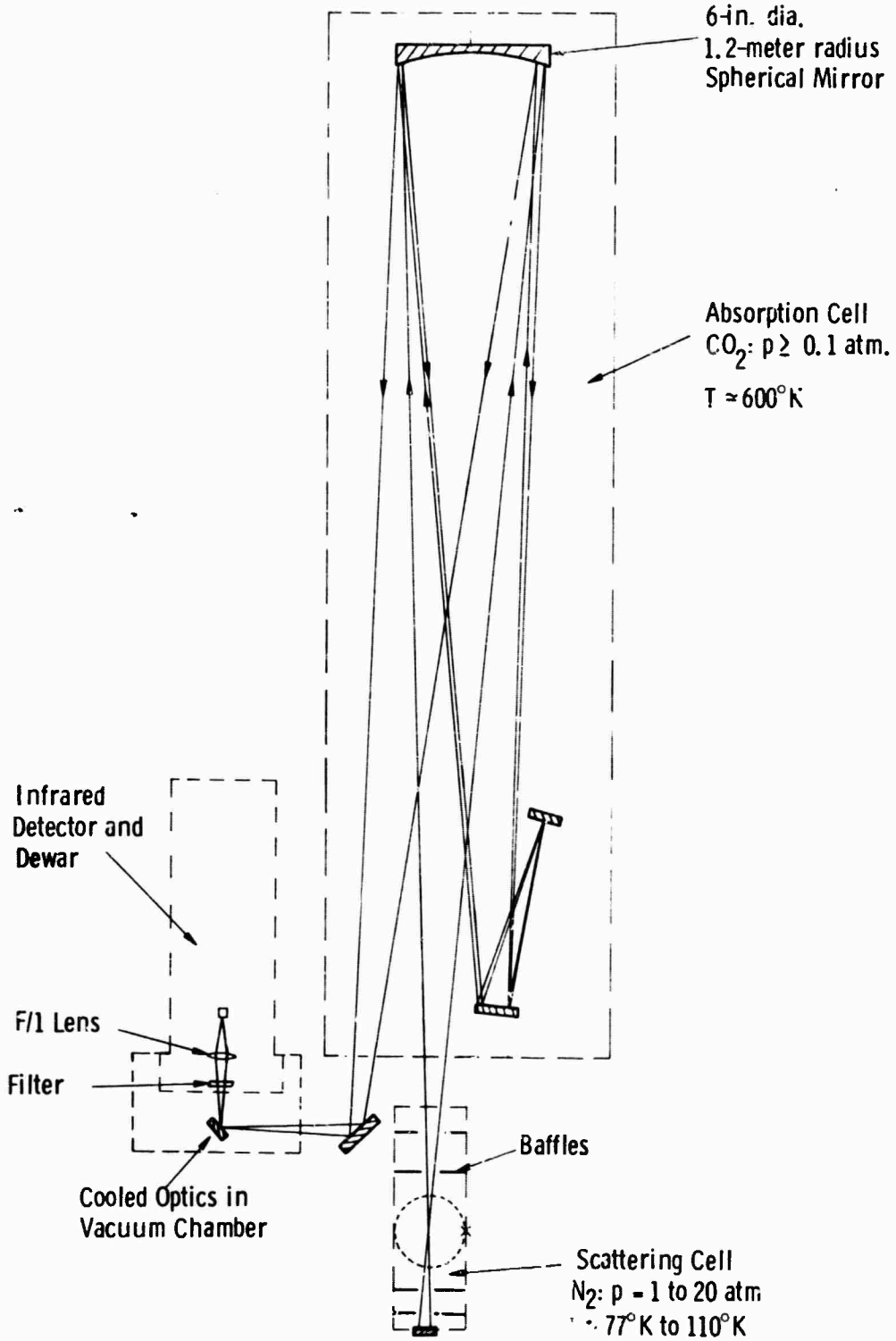

Fig. 3. IR Detection System.

50 megawatts. For the 200-nanosecond pulse, the laser pulse has 10 joules energy. The intracavity option shown in Fig. 2B operates at about 625 megawatts output: corresponding to about 125 joules-per-pulse. To date, we have obtained measurements by using only the system shown in Fig. 2A.

The special requirements on the optical/detection system for this experiment are

1. Suppression of scattered radiation at the 10.6-micron laser line (i.e., separation of the Raman-scattered radiation from the primary beam);
2. Suppression of scattered radiation from the wall and dust in the gas, particularly severe due to the low Raman scattering cross section; and
3. Sufficient sensitivity to observe Raman-scattered radiation.

The first requirement will be met by employing a linearly polarized CO_2 laser beam and the Raman scattered radiation will be observed in a direction parallel to the polarization vector in the incident laser beam. Thus, in Fig. 2, the polarization vector is in the plane of the paper. This technique reduces both the Rayleigh- and Raman-scattered intensities by a factor equal to the depolarization ratio, ρ. However, for Rayleigh scattering in N_2, $\rho_{Rayleigh} = 1.2 \times 10^{-2}$; while for pure rotation Raman scattering, $\rho = 0.75$[1]. Similarly, for O_2, $\rho_{Rayleigh} = 1.4 \times 10^{-2}$, and $\rho_{Raman} = 0.75$.

A further reduction in the 10.6-micron scattered radiation is achieved by allowing the scattered radiation to pass through a cell containing pure CO_2 gas at 600 to 700°K and 0.10 atmosphere pressure. The gas acts as a filter to remove both the Rayleigh scattered radiation and the 10.6-micron radiation scattered from the dust in the gas and from the wall. As shown in Fig. 3, this absorption cell provides a 400-cm optical path length.

The transmission at the center of the P(20) line of CO_2 at 10.6 microns is plotted in Fig. 4 as a function of gas temperature.[2] Above about 5×10^{-2} atmospheres of CO_2, the line becomes purely collision-broadened, so that the curve shown in Fig. 4 is independent of gas pressure above 10^{-1} atmosphere. Note that for the 4 meter path, the CO_2 gas attenuates radiation at the laser line by 10^{-3} and 10^{-4} at the respective CO_2 temperatures of 600 and $700^{o}K$.

Besides the filtering by the CO_2 absorption cell, suppression of scattered radiation from the walls is achieved by employing a series of diaphragm baffles in the scattering chamber.

When N_2(or O_2) is the scattering chamber and CO_2 is in the absorption cell, the above apparatus can measure the Raman-scattered radiation from N_2(or O_2) into the IR detector.

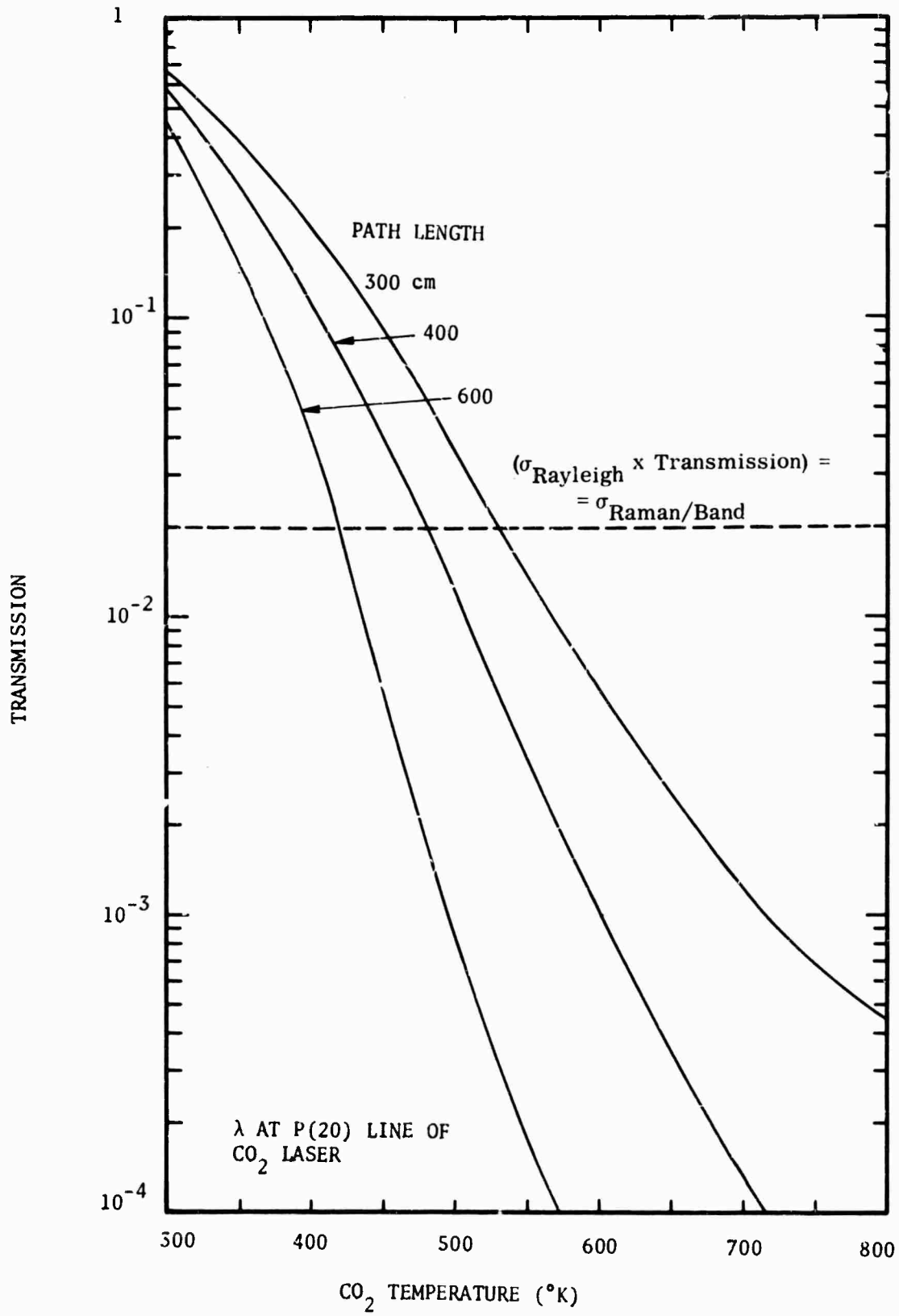

Fig. 4. Transmission Through CO_2 at 10.6μ.

3. EXPERIMENTAL MEASUREMENTS

To date, the measurement program consists of the calibration measurements on the infrared detection system and the measurements made to evaluate the effects of scattered radiation from the walls and from the particles in the gas.

The infrared detection system is calibrated in static and dynamic tests. The experimental arrangements for these two calibrations are shown in Fig. 5. The optical system is the same for both calibrations, except for the addition of a plane mirror in the static calculation for observations of the blackbody source. In the dynamic calibration, the laser beam traverses the scattering chamber that contains pure CO_2 at pressures between 1 torr and 1 atmosphere. Absorption by the CO_2 excites the ν_3 mode that subsequently radiates in the 4.3-, 9.4-, and 10.4-micron bands. The static calibration serves as a direct check on the sensitivity of the detection system because the blackbody emission is well known. The dynamic calibration serves to calibrate the operation of the laser/optical system. The CO_2 emission also serves as the reference with which to compare the Raman scattering emission. This comparison eliminates the requirements for knowing the (1) laser-beam geometry, (2) optical system throughput, and (3) detector sensitivity.

3.1. Static Calibration of Infrared System

Figure 6 shows the transmission of the filter placed in front of the Ge:Hg liquid-helium-cooled detection system. To calibrate the infrared system, the filter transmission curve must be folded into the incident spectral intensity. A blackbody source at different temperatures is used. The response of the system to blackbody radiation is determined as follows: Let the blackbody spectral intensity be $B(\lambda)d\lambda$, the optical system throughput, including the lens and filter be $F(\lambda)$, and the response of the cell be $R(\lambda)$. R is essentially constant over the bandpass of the filter. The output, V, of the detection system is defined by

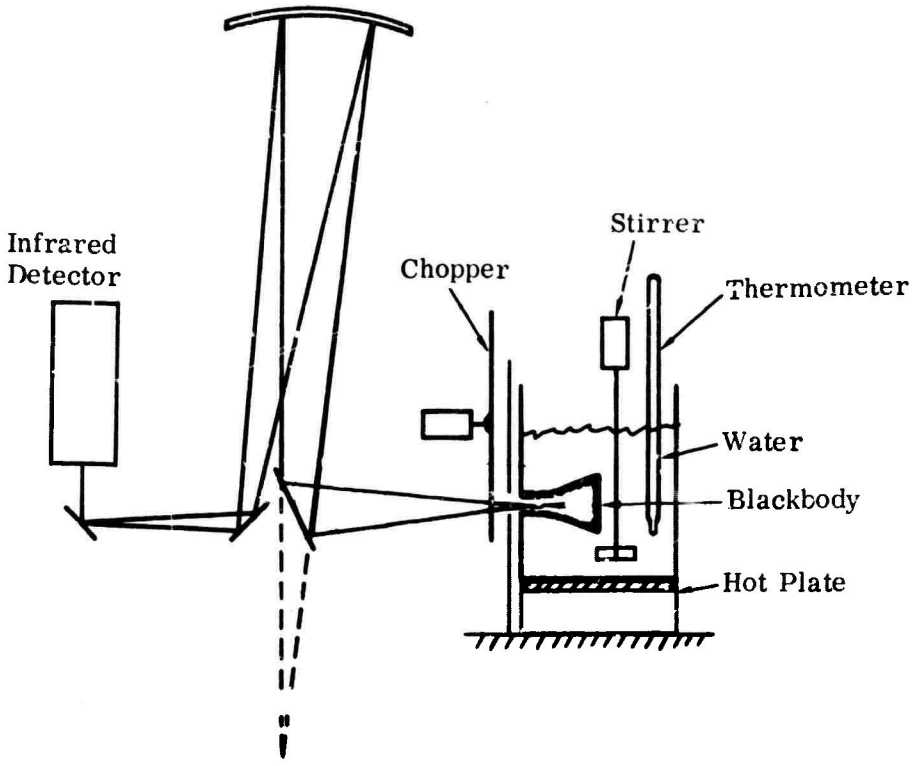

Fig. 5a. Experimental Arrangement for Static Calibration.

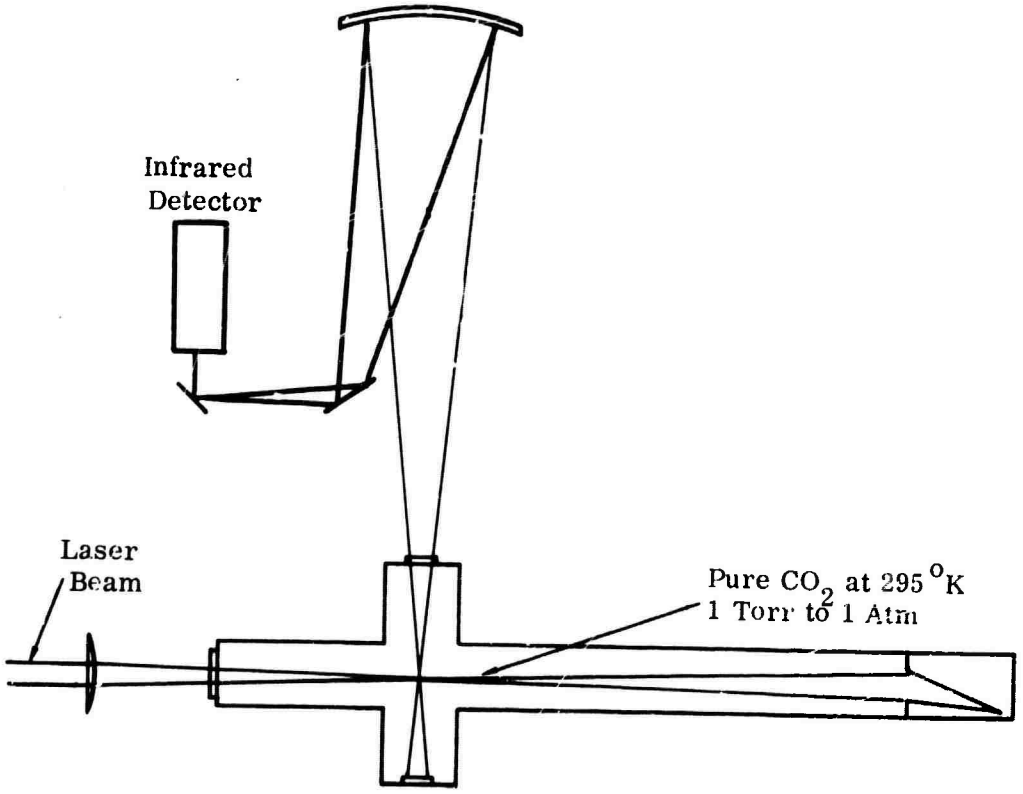

Fig. 5b. Experimental Arrangement for Dynamic Calibration.

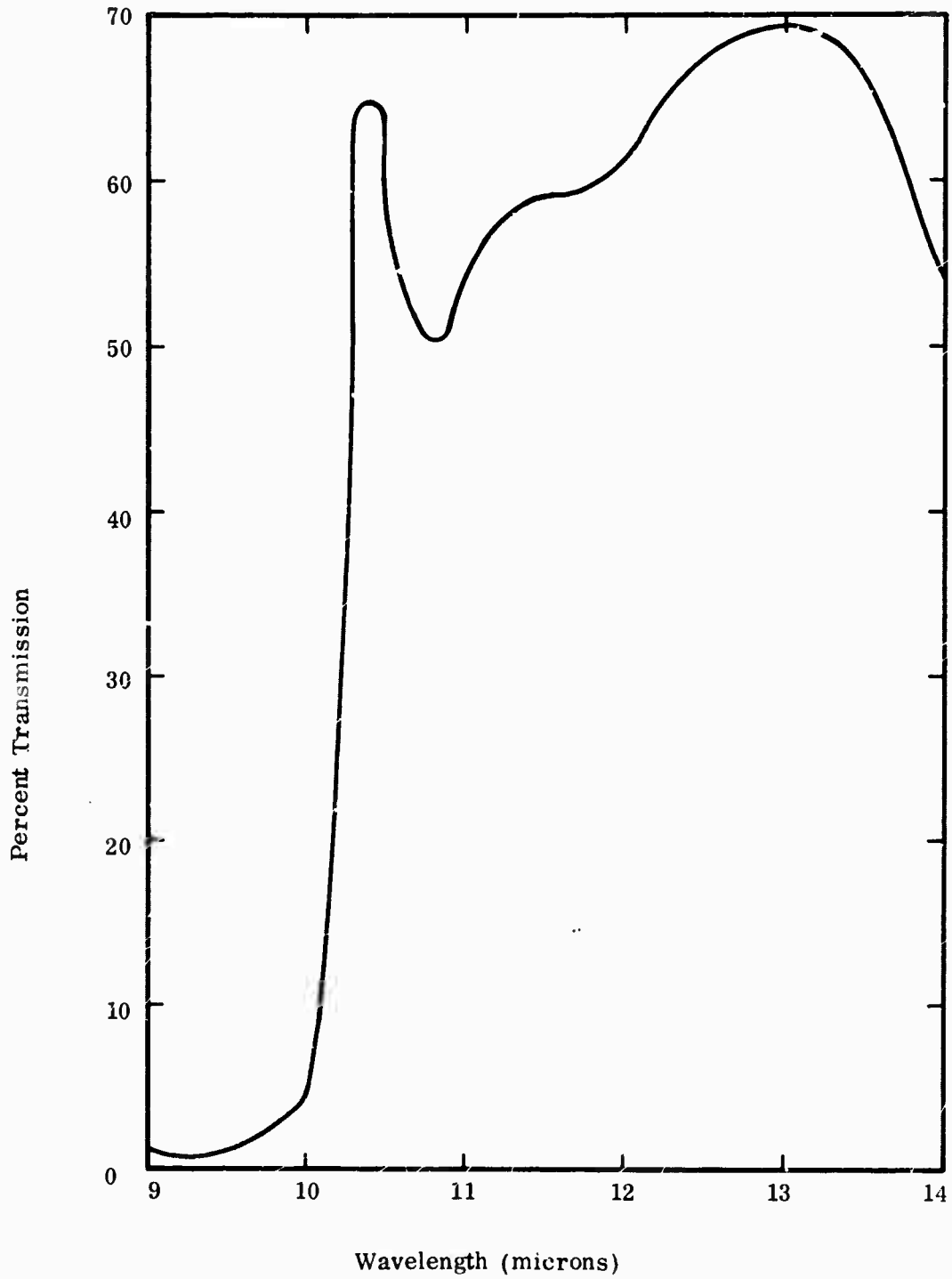

Fig. 6. Spectral Transmission of IR Filter.

$$V' = R \int_0^\infty F(\lambda)\, B(\lambda)\, d\lambda \quad , \tag{2}$$

where R is the calibration constant to be determined.

The calibration procedure consists of varying the infrared light incident on the detector by varying the blackbody temperature and measuring the output, V. In addition, the integral in Eq. (2) is evaluated over the same temperature range.

The experimental setup is shown schematically in Fig. 5a. A tank with a flask painted dull black on the inside serves as the blackbody. The blackbody temperature is controlled by varying the temperature of the water surrounding the flask. The fluid is kept in constant agitation so that the temperature of the bath is uniform throughout the container. The radiation coming from inside the flask is imaged on the infrared cell. A light chopper is placed in front of the source. The AC output of the infrared system is

$$V_{BB} = R \int_0^\infty F\, B\, d\lambda \; - V_c \quad , \tag{3}$$

where V_c is the signal with the chopper wheel closed. The chopper wheel is painted black to minimize reflections from its surface. Thus, V_c is due to thermal radiation from the chopper wheel. Consequently, Eq. (3) becomes

$$V_{BB} = R \int_0^\infty F(B - B_0)\, d\lambda \quad , \tag{4}$$

where B_0 is the blackbody emission at the chopper-wheel temperature.

A typical calibration oscilloscope measurement is shown in Fig. 7. Figure 8 shows the measured output of the infrared system in millivolts plotted as a function of the blackbody temperature in ^{o}C. Note that the signal is zero

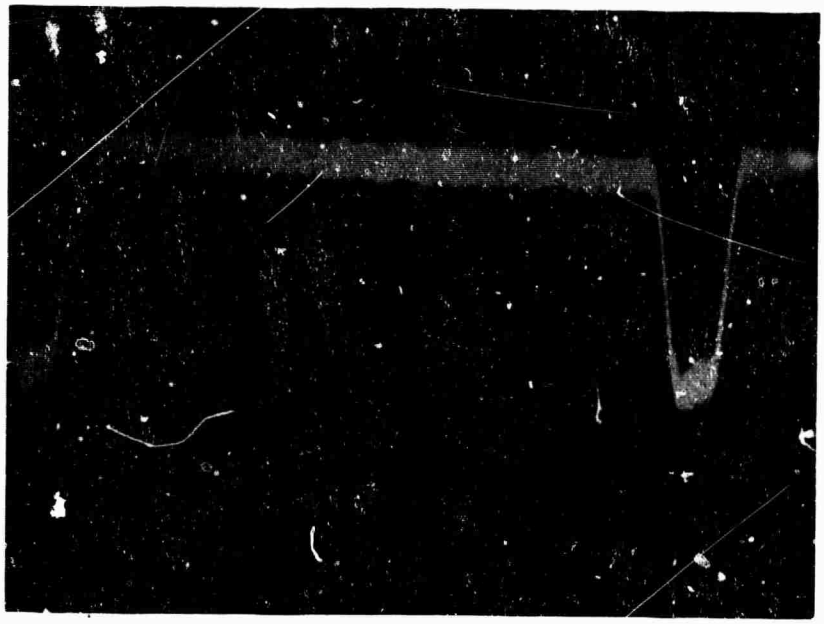

a. 20 mV/cm, 5 ms/cm. T = -12.5°K

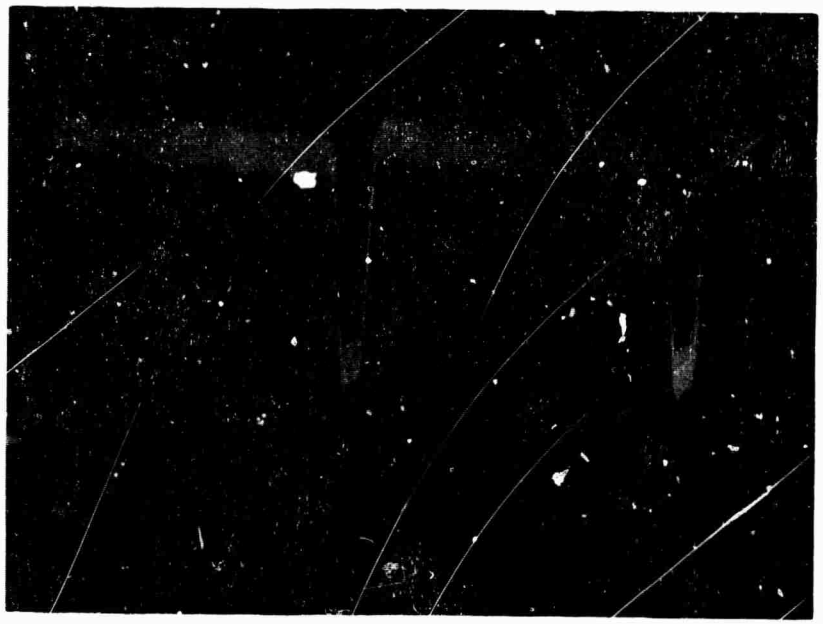

b. 20 mV/cm, 10 ms/cm. T = -12.5°K

Fig. 7. IR Static Calibration. Detector Response to Blackbody Source.

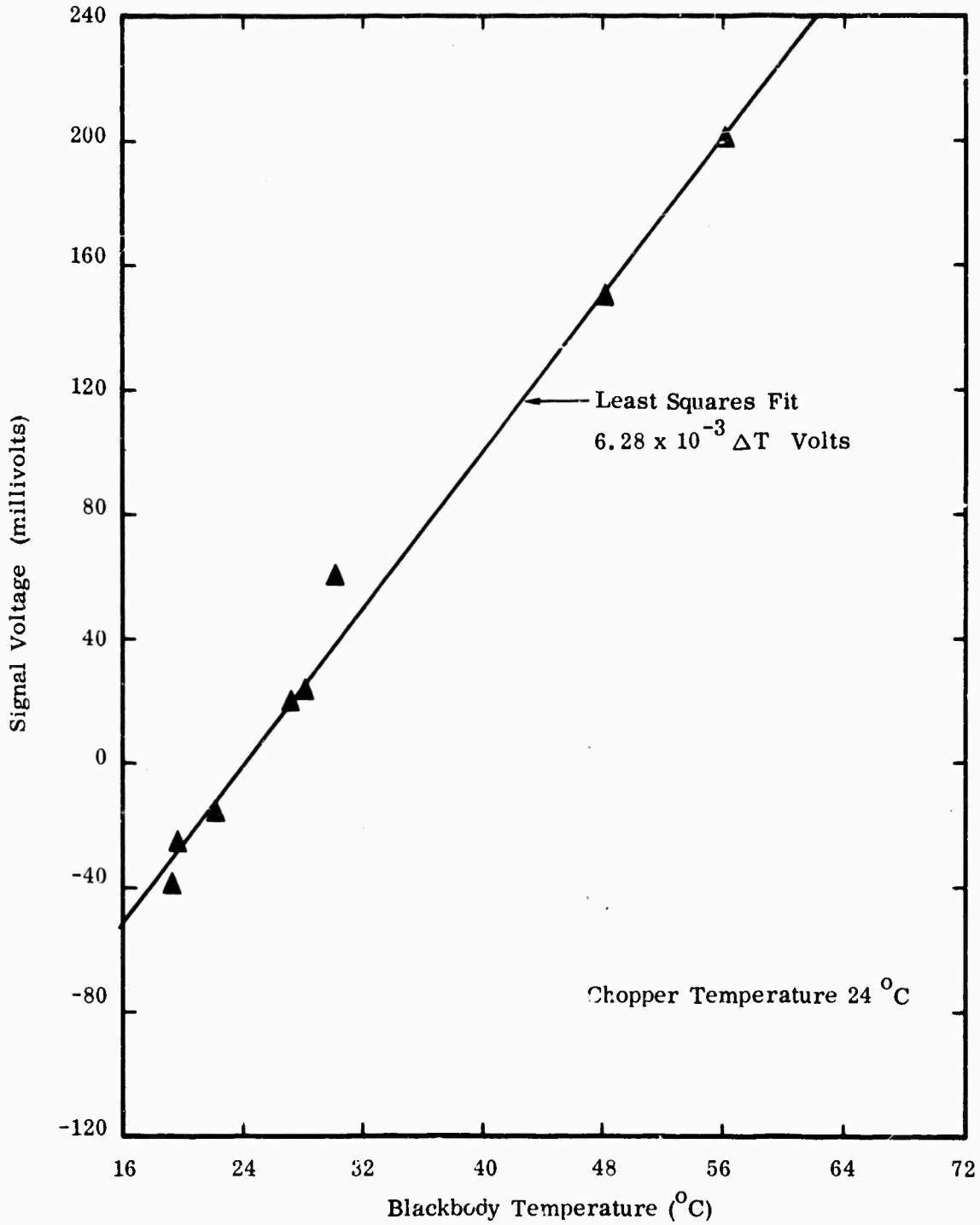

Fig. 8. Results of Static Calibration of IR Detection System.

at 24°C, which is the chopper-wheel temperature. At higher temperatures, the output is positive; while at lower temperatures, it is negative.

The infrared system calibration consists of 1) correlating measurements, as shown in Figs. 7 and 8, with theoretical calculations of the detector system output given by Eq. (3), and 2) determining the responsivity. For a chopper temperature of 24°C, the integral in Eq. (4) has the value

$$\int_0^\infty F(B - B_0)d\lambda = 3.45 \times 10^{-5} \Delta T \quad \text{watts/cm}^2\text{-sr} \quad ,$$

so that the responsivity of the system is

$$R = 2.90 \times 10^4 \frac{V_{BB}}{\Delta T} \qquad \text{volts/watts-cm}^{-2}\text{-sr}^{-1} \quad .$$

The quantity ΔT is the temperature difference between the blackbody source and the chopper wheel. The measured signal voltage V_{BB} as seen in Fig. 8 is linear in ΔT so that the responsivity R is independent of ΔT. For the data shown in Fig. 8,

$$V_{BB} = 6.28 \times 10^{-3} \quad \Delta T \quad , \tag{5}$$

so that

$$R = 1.82 \times 10^2 \quad \text{volts/watts-cm}^{-2}\text{-sr}^{-1} \quad . \tag{6}$$

The principal contribution to the noise level in the system is from shot noise in the infrared detector and its bias circuit. The Ge:Hg detector at 4.2°K has a resistance of 180 K ohms, and is biased by 45 volts and a 100K ohm load. The resulting shot noise is

$$V_N = G\left[2q\, i_{dc}\, f(R_D^2 + R_L^2)\right]^{1/2} \quad , \tag{7}$$

where i_{dc} is the dc current through the detector; f is the bandwidth of the system; G = 17 is the voltage gain of the amplifier; and R_D and R_L are the respective resistances of the detector and load. For the bias circuit described, $i_{dc} = 1.61 \times 10^{-4}$ amperes, so that the noise is

$$V_N = 2.5 \times 10^{-5} f^{1/2} \quad \text{volts.} \tag{8}$$

The electrical bandwidth was determined experimentally by measuring the rise time of the complete electrical system with the cooled detector installed. The system 1/e risetime was 0.375 μsec, which corresponds with a bandwidth of 0.42 MHz. Consequently, the noise voltage is

$$V_N = 1.6 \times 10^{-2} \text{ volts.} \tag{9}$$

This noise level is consistent with the measurements shown in Fig. 7. Combining this noise level with Eq. (5) then yields the signal-to-noise ratio for the static calibration as

$$S/N = V_{BB}/V_N = 0.39 \quad \Delta T \quad .$$

Therefore, the signal-to-noise ratio is unity for $\Delta T = 2.6^{\circ}C$.

3.2 Dynamic Calibration of Infrared System

The dynamic calibration employed the experimental arrangement shown in Fig. 5b. The scattering chamber was filled with CO_2 at pressures from about 8 torr to 1 atmosphere. A laser beam at several joules per pulse was focused at the center of the tube with a one meter lens. The focusing was not as good as the best when we previously measured a beam spot size of 4 mm. For the calibration, the beam cross-section diameter at the focal point was 8 mm; this is depicted in Fig. 9, which shows the spot burned on exposed Polaroid film by the laser beam at the point where the optical system observes the laser beam.

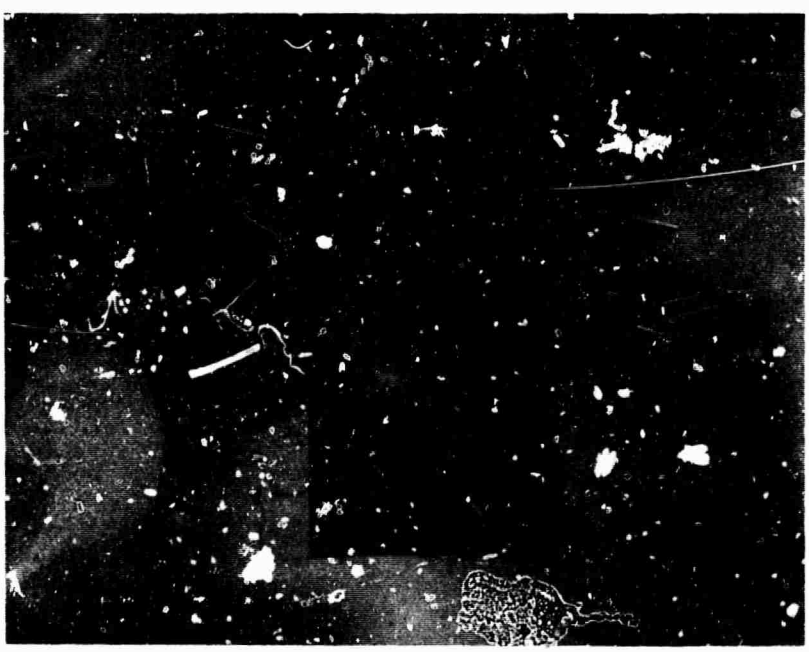

Fig. 9. Laser Spot Size (Full Scale) for Preliminary Data from CO_2 Dynamic Calibration.

The dynamic calibration measurements enable us to make a preliminary judgment of the performance of the experimental system. In particular, we observed the radiation from CO_2 at 10 microns excited by the laser beam, and from this, we can make direct predictions of the sensitivity of the experimental system to observe the Raman scattering. There is no need for absolute measurements, as the intent of this experiment is to make a relative measurement of the Raman scattering with respect to the CO_2 emission. The CO_2 emission can also be compared with the other sources of radiation that are obtained from the walls of the scattering chamber, as well as to the radiation scattered from dust. In these preliminary measurements, there were no baffles in the scattering chamber, neither along the laser beam, nor in the direction of the optical detection system. However, a Mylar conical horn was placed at an angle about 140 cm downstream of the observed scattering volume that collected and dissipated the laser energy. Apparently the backscattering from this horn was quite small, and the radiation scattered in the direction of the optical system was much less than expected. In fact, it is low enough that one can almost use the simple hot CO_2 absorber alone in the detection system to eliminate that level of scattering. The scattering from the dust in the gas was not observed, even operating at one atmosphere. Apparently the tank of CO_2 was quite pure and did not have sufficiently large-diameter particles to increase substantially the observed background radiation. At vacuum or at one atmosphere pressure, the observed background radiation was due to the wall scattering.

Before presenting the experimental measurements, we shall describe the expected shape of the signal with CO_2 in the scattering chamber. If the scattering chamber were filled with pure CO_2, then irradiation by a CO_2 laser would produce absorption by the CO_2 molecules. The detector monitoring the gas (with an evacuated absorption cell in front of the detector) immediately after the laser pulse would measure the 9.4- and 10.6-micron radiation emitted by the vibrationally excited $CO_2(00^01)$ molecules. Since the absorption cross section for the $CO_2(10^00)$ state and the radiative lifetime of the $CC_2(00^01)$ state are well known, this measurement calibrates the apparatus and essentially yields a Raman scattering cross section for N_2 relative to the absorption cross section of CO_2 at 10.6 microns.

In this calibration procedure, the CO_2 gas pressure is set to yield a signal at the detector comparable in intensity to the Raman-scattered signal. The calibration is run under the same conditions as the Raman scattering experiment. The laser operating parameters, the detection system, and the wavelength of the radiation are all kept the same in both cases.

During the laser pulse, the population of the CO_2 (00^01) state increases by

$$CO_2(10^00;\ J = 20) + h\nu \rightarrow CO_2(00^01,\ J = 19) \quad .$$

The incident laser power density is sufficiently high in this apparatus ($P_f \simeq 4 \times 10^8$ watts/cm^2) to saturate the absorbing $CO_2(10^00;J = 20)$ level. Consequently, at the end of the laser pulse, the population of the entire $CO_2(00^01)$ vibrational state is equal to the population of each vibrational state coupled to the $CO_2(10^00)$ state. At 300°K, this coupling is due to the following reactions:

$$CO_2(02^0 0) + CO_2 \xrightarrow{k_1} CO_2(10^0 0) + CO_2 - 102\ cm^{-1}$$

$$CO_2(02^2 0) + CO_2 \xrightarrow{k_2} CO_2(10^0 0) + CO_2 - 52\ cm^{-1}$$

$$CO_2(01^1 0) + CO_2(01^1 0) \xrightarrow{k_3} CO_2(02^2 0) + CO_2(00^0 0) - 2\ cm^{-1} \quad .$$

As quoted by Taylor and Bitterman,[3] the rate constants and the corresponding characteristic times for these processes are

$$k_1 = 1.9 \times 10^{-11}\ cm^3/sec; \qquad \tau_1 = \frac{2.2 \times 10^{-9}}{p_{CO_2}}\ sec$$

$$k_2 = 2.3 \times 10^{-11}\ cm^3/sec; \qquad \tau_2 = \frac{1.7 \times 10^{-9}}{p_{CO_2}}\ sec$$

$$k_3 = 1.5 \times 10^{-11}\ cm^3/sec; \qquad \tau_3 = \frac{6.7 \times 10^{-8}}{p_{CO_2}}\ sec \quad .$$

Repopulation of the $CO_2(02^0 0)$ and $CO_2(02^2 0)$ states by

$$CO_2(01^1 0) + CO_2 \rightarrow CO_2(02^0 0 \text{ or } 02^2 0) + CO_2$$

has a characteristic time of 90 μsec at p_{CO_2} = 1 atm and, consequently, is not of importance during the 0.2-μsec laser pulse. The repopulation of the $CO_2(01^1 0)$ state from the ground state is even slower ($\simeq$ 180 μsec at p_{CO_2} = 1 atm), so that the $CO_2(10^0 0)$ state is effectively decoupled from the ground state.

The rate constants listed above indicate that for $p_{CO_2} > 0.10$ atm, the population of the $CO_2(00^0 1)$ state is given by

$$[CO_2(00^01)] = [CO_2(10^00)] = [CO_2(02^00)] \exp[-(E_{10^00} - E_{02^00})/kT]$$

$$= [CO_2(02^20)] \exp[-(E_{10^00} - E_{02^20})/kT]$$

$$= [CO_2(01^10)] \exp[-(E_{10^00} - E_{01^10})/kT] \quad .$$

Coupled with the fact that

$$[CO_2(00^01)] + [CO_2(10^00)] + [CO_2(02^00)] + [CO_2(02^20)] + [CO_2(01^10)]$$

$$= \{[CO_2(00^01)] + [CO_2(10^00)] + [CO_2(02^00)]$$

$$+ [CO_2(02^20)] + [CO_2(01^10)]\}_{equil} \quad ,$$

one finds that the $CO_2(00^01)$ concentration at the end of the laser pulse is

$$[CO_2(00^01)]_f = 0.69\,[CO_2(10^00)]_{equil}$$

$$= 2.4 \times 10^{16} p_{CO_2} \qquad (10)$$

at $300^\circ K$. In Eq. (10), the CO_2 pressure is in atmospheres.

For $p_{CO_2} \leq 0.10$ atm, the $CO_2(00^01)$ concentration is given by a similar expression, except with no contribution from the $CO_2(01^10)$ state, since at such low pressure, the $CO_2(01^10)$ state is decoupled from the $CO_2(02^00)$ and $CO_2(02^20)$ states during the laser pulse. Consequently, for $p_{CO_2} \lesssim 0.10$ atm,

$$[CO_2(00^01)]_\ell = 0.85 \left[CO_2\,(10^00)\right]_{equil}$$

$$= 2.9 \times 10^{16}\, p_{CO_2} \quad . \tag{11}$$

During the interval immediately following the laser pulse, the $CO_2(00^01)$ population is decreased by

$$CO_2(00^01) + CO_2 \xrightarrow{k} CO_2 + CO_2$$

$$CO_2(00^01) + h\nu \xrightarrow{\tau_{10.6}} CO_2(10^00) + h\nu$$

$$CO_2(00^01) + h\nu \xrightarrow{\tau_{9.4}} CO_2(02^00) + h\nu$$

$$CO_2(00^01) + h\nu \xrightarrow{\tau_{4.3}} CO_2 + h\nu \quad ,$$

where the radiative lifetimes are $\tau_{10.6} \simeq \tau_{9.4} = 4.7$ sec, and $\tau_{4.3} = 3 \times 10^{-3}$ sec, and the rate constant $k \simeq 4 \times 10^{-15}$ cm^3/sec at 300^{o}K.[3] Therefore, after the CO_2 laser pulse, the CO_2 excited state population is

$$\left[CO_2(00^01)\right] = \left[CO_2(00^01)\right]_\ell e^{-t/\tau} \quad , \tag{12}$$

where

$$1/\tau = k\left[CO_2\right] = 10^5\, p_{CO_2} \quad .$$

The 10.4-micron band emission from the laser excited CO_2 is observed by the infrared detection system. The voltage output of the system is given by the relation

$$V_{CO_2} = RF \frac{d}{4\pi} \frac{h\nu}{\tau_r} [CO_2(00^01)]_\ell \, e^{-t/\tau} \quad , \tag{13}$$

where R is given by Eq. (6), F is the mean filter transmission at the detector (F = 0.60), d is the effective diameter of the CO_2 gas volume emitting radiation, and τ_r = 4.7 sec is the radiative lifetime. For the calibration measurements run to date, d = 0.8cm. By using Eq. (6) for R and Eq. (10) or (11) for $[CO_2(00^01)]$, the voltage output becomes

$$V_{CO_2} = \begin{cases} 7.1 \times 10^{-4} \, p_{CO_2} \, e^{-t/\tau} & p_{CO_2} > 1/3 \text{ atm} \\ \\ 8.6 \times 10^{-4} \, p_{CO_2} e^{-t/\tau} & 1/30 \text{ atm} < p_{CO_2} < 1/3 \text{ atm} \end{cases} \quad . \tag{1}$$

When comparing Eq. (14) with Eq. (9), the predicted signal-to-noise ratio for this measurement becomes

$$\left(\frac{S}{N}\right)_{CO_2} = \begin{cases} 0.04 \, p_{CO_2} e^{-t/\tau} \; ; & p_{CO_2} > 1/3 \text{ atm} \\ \\ 0.05 \, p_{CO_2} e^{-t/\tau} \; ; & 1/30 \text{ atm} < p_{CO_2} < 1/3 \text{ atm} \end{cases} \quad . \tag{15}$$

For the calibration runs to date, an f/1 lens was used in front of the infrared detector to increase the source area and the responsivity by a factor of 16. In addition, the interference filter was not used, so that the emission from both the 9.4- and 10.4-micron bands of CO_2 were observed. Consequently, for these calibration runs, the signal given by Eq. (14) and the signal-to-noise ratio given by Eq. (15) must be multiplied by the factor $16(1/0.60)2 = 53.3$. The resulting signal-to-noise ratio is then

$$\left(\frac{S}{N}\right)_{CO_2} = \begin{cases} 2.1\, p_{CO_2} e^{-t/\tau} & p_{CO_2} > \frac{1}{3}\,\text{atm} \\ 2.7\, p_{CO_2} e^{-t/\tau} & \frac{1}{30}\,\text{atm} < p_{CO_2} < \frac{1}{3}\,\text{atm} \end{cases} \quad . \tag{16}$$

Several oscillograms showing the observed radiation from the scattering chamber containing CO_2 are displayed in Fig. 10. Figure 10A was taken with a vacuum in the chamber; Fig. 10B at 17 torr; Fig. 10C at 100 torr and Fig. 10D at 500 torr. Note the large off-scale spike at the beginning of the trace. This spike is due to wall-scattered radiation that dominates the initial signal. After several microseconds, the system recovers, and the residual radiation is due to the CO_2 emission. Note the variation of relaxation times with pressure, and the lack of a residual signal in the vacuum data. Since pure CO_2 is used, one obtains a rate constant for deactivating the CO_2 (00^01) state in CO_2 collision. An analysis of data indicates a rate constant of 1×10^{-14} cc/sec, which agrees with the rate constant reported in the literature.

3.3 Predicted Signal- to-Noise Ratio for Raman Scattering Measurements

The signal-to-noise ratio for the high pressure CO_2 runs, extrapolated to zero time, is of the order of 30. This ratio is about a factor of ten greater than the predictions of Eq. (16). Even though this data represents the initial preliminary runs, we shall use it to make predictions of the Raman-scattered radiation from N_2 and O_2.

The Raman scattered radiation incident on the infrared detector produces the voltage

$$V_R = RFdP_\ell\, \sigma_R [N_2] \quad , \tag{17}$$

a. 10 mV/cm, 10μsec. Vacuum.

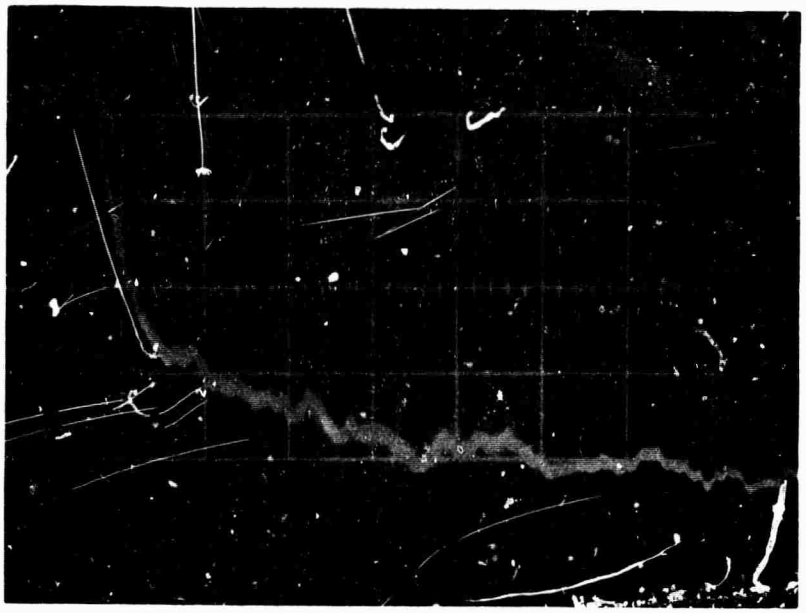

b. 5 mV/cm, 50 μsec/cm. 17 Torr of CO_2

Fig. 10. CO_2 Dynamic Calibration

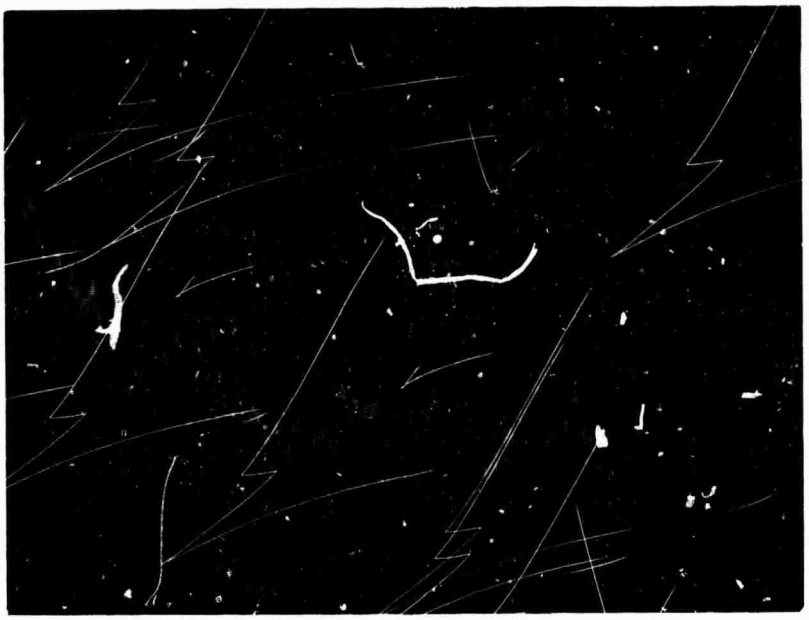

c. 10 mV/cm, 20 μsec/cm. 100 Torr of CO_2.

d. 10 mV/cm, 10 μsec/cm. 500 Torr of CO_2

Fig. 10. CO_2 Dynamic Calibration (continued)

where V_R is the detector signal in volts, σ_R is the total Raman scattering cross section per steradian, and $[N_2]$ is the nitrogen number density. The number density $[N_2]$ can be expressed in terms of pressure as

$$[N_2] = p_{N_2} L_o \left(\frac{273\,^oK}{T_{N_2}} \right) , \tag{18}$$

where p_{N_2} is the gas pressure in atmospheres, L_o is 2.7×10^{19} and T_{N_2} is the temperature in degrees Kelvin. By inserting Eq. (18) into Eq. (17),

$$V_R = RFd\, P_\ell\, \sigma_R\, L_o\, p_{N_2} \left(\frac{273\,^oK}{T_{N_2}} \right) . \tag{19}$$

The Raman-scattered cross section can be determined relative to the CO_2 absorption cross section and radiative lifetime at 10.6 microns by taking the ratio of the Raman-scattered intensity to the CO_2 emission, Eq. (13) and (19); i.e.,

$$\frac{V_R}{V_{CO_2}} = 4\pi \left(\frac{\tau_r}{h\nu} \right) P_\ell\, \sigma_R \frac{L_o p_{N_2} (273/T_{N_2})}{[CO_2(00^o1)]_\ell} e^{t/\tau} , \tag{20}$$

where $[CO_2(00^o1)]_\ell$ is given by Eq. (10) or (11). Note that neither the responsivity of the optical system nor the CO_2 absorption coefficient enters Eq. (20). At CO_2 pressure below 10^{-1} atmospheres, $1/\tau < 10^4$ so that $e^{-t/\tau} \simeq 1$ to better than 1 percent for observation times of the order of 10^{-6} sec. Under these conditions,

$$\frac{V_R}{V_{CO_2}} = 4\pi \left(\frac{\tau_r}{h\nu} \right) P_\ell \sigma_R \frac{L_o p_{N_2}}{[CO_2(00^o1)]_\ell} \left(\frac{273}{T_{N_2}} \right) . \tag{21}$$

By varying the CO_2 gas pressure at a fixed temperature, this ratio can have a value near unity for suitable values of the nitrogen parameters. For example, when using $\sigma_R = 8 \times 10^{-35} cm^2/sr$ and $P_\ell = 4 \times 10^8$ watts/cm^2, for 10 atmospheres of N_2 at 110°K, $V_R/V_{CO_2} = 2.6$ at 1 atm of CO_2, while for 0.67 atm of CO_2, $V_R/V_{CO_2} \simeq 4.0$.

These results, combined with our preliminary analysis of the dynamic calibration data, permit us to estimate the sensitivity of the optical system for detection of the Raman signal. The signal-to-noise ratio for the Raman signal is given by

$$\left(\frac{S}{N}\right)_R = \left(\frac{S}{N}\right)_{CO_2} \left(\frac{F}{2}\right) \frac{V_R}{V_{CO_2}} \quad . \tag{22}$$

The factor F/2 appears in Eq. (22), since the signal-to-noise ratio for CO_2 was determined experimentally without the spectral filter in front of the detector, and allows the emission from both the 9.4- and 10.4-micron bands of CO_2 to be measured. However, Eqs. (20) and (21) assume the filter is used in both the Raman and the CO_2 emission measurements.

For the CO_2 data taken at approximately 0.67 atmosphere, the measured signal-to-noise ratio was approximately 30. Thus for the Raman signal at 10 atmospheres of N_2 at 110°K,

$$\left(\frac{S}{N}\right)_R = (30)(0.67/2)(4)(0.10) = 3.6 \quad . \tag{23}$$

The factor of 0.10 is included since the CO_2 data were taken with $P_\ell \sim 4 \times 10^7 w/cm^2$. Better focusing of the laser beam would increase P_ℓ to 4×10^8 w/cm^2. Two further increases in signal can be obtained by: (1) inserting a mirror at the bottom of the scattering cell to reflect the scattered radiation into the detection system to increase the signal by a factor of 2; and (2), performing the experiment

inside the laser cavity to provide a factor of 12.5 increase in an available laser energy. When applying these two factors to Eq. (23), the Raman signal-to-noise ratio becomes

$$\left(\frac{S}{N}\right)_R = (36)(2)(12.5) = 900 \quad . \tag{24}$$

3.4. Wall and Dust Scattering Measurements

Another important result that can be obtained from the dynamic calibration is the seriousness of the wall and dust scattering. The signal level observed during the laser pulse was of the order of 10^3 times larger than the CO_2 level, and the CO_2 emission was masked during the laser pulse. This large signal was monitored at different CO_2 pressures and was independent of the CO_2 pressure, indicating that the radiation came from the walls of the chamber. Even at one atmosphere CO_2 pressure, additional radiation from the gas was not observed. Now, since the radiation from the walls was 10^3 times the CO_2 level, the wall-scattered radiation can be easily treated. At high nitrogen pressure, the Raman scattering is comparable to the CO_2 signal. Thus, the wall radiation is about 10^3 times larger than the Raman scattering. With the CO_2 absorption cell in the optical path, the Raman scattering would be less than the wall radiation, and this is without any baffles in the scattering chamber. It is expected that a set of baffles along the optical detection system could easily reduce the radiation by several orders of magnitude. Thus, the suppression of background radiation with this system does not appear to be a severe problem. However, these measurements are preliminary, and more detail work is required.

3.5 Modifications to the Experimental Apparatus and Proposed Work

Since the preliminary data were taken, two major improvements have been incorporated into the experimental system: the first one involved the detector electronics and the second concerned baffles for the optical system.

The bias circuit for the infrared detector and the amplifier have been modified to yield a faster risetime and a lower noise voltage. At present, the infrared detector and its amplifier have a combined 1/e risetime of 2×10^{-8} sec, corresponding to a bandwidth of 8 MHz. This is a substantial improvement over the previous value of 0.42 MHz, and it allows the detector to monitor faithfully the incident laser pulse. This fact is borne out in the photographs shown in Fig. 11. Figure 11a shows the output from a photon drag detector (90% risetime less than 10^{-9} sec) monitoring the CO_2 TEA laser pulse. Figure 11b shows the laser radiation scattered from the walls of the evacuated cell as monitored by the infrared detector. In both cases, the shape of the laser pulse, including its initial maximum, is the same. Thus the detector electronics have been improved to the point where they can monitor scattered radiation during the laser pulse.

Compared with the 16 millivolts previously reported, the shot noise in the circuit has been reduced to yield approximately 3 millivolts of noise.

Work was also begun on reducing the wall scattering in the cell by use of suitable baffles. As observed initially, and as reported earlier in this report, the signal due to wall scattering was of the order of 10^3 times greater than the corresponding signal due to CO_2 emission. However, with the use of the baffle system shown in Fig. 12, the wall scattering signal has been reduced to approximately 10 times the electrical noise. The most critical baffles in the system are: (1) the baffle farthest upstream in the scattering cell; (2) the baffle immediately downstream of the cross in the cell; and (3) the two baffles in the upper vertical arm of the cell. The effects of these baffles can be seen in Fig. 13a, which shows the wall scattered radiation from the evacuated cell. The maximum value of S/N is approximately 10.

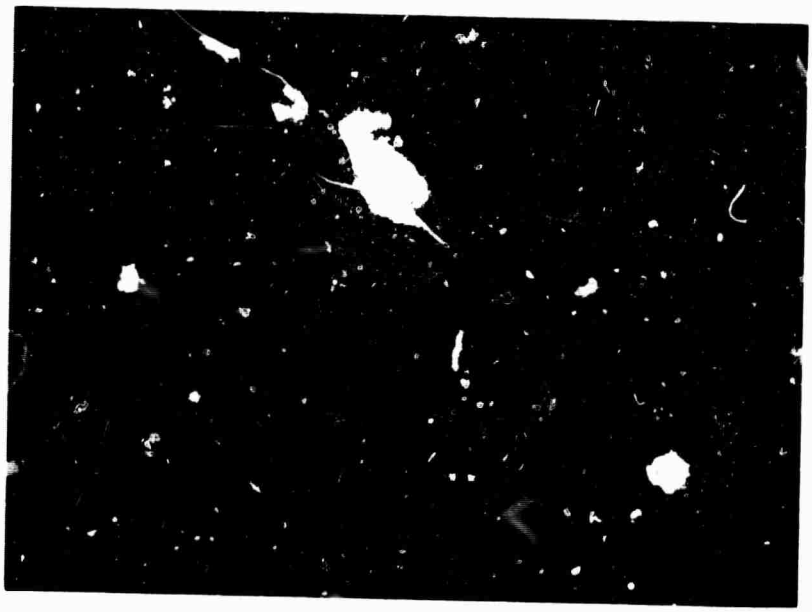

a. Photon Drag Detector Output. 5 mV/cm, 0.2 μsec/cm

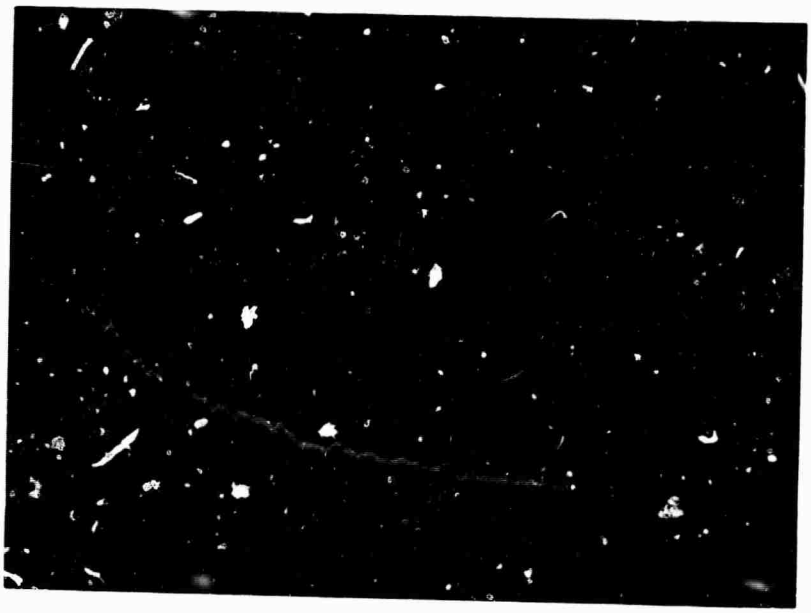

b. Infrared Detector Output of Wall Scattered Laser Radiation. 10 mV/cm, 0.5 μsec/cm.

Fig. 11. TEA Laser Pulse Shape

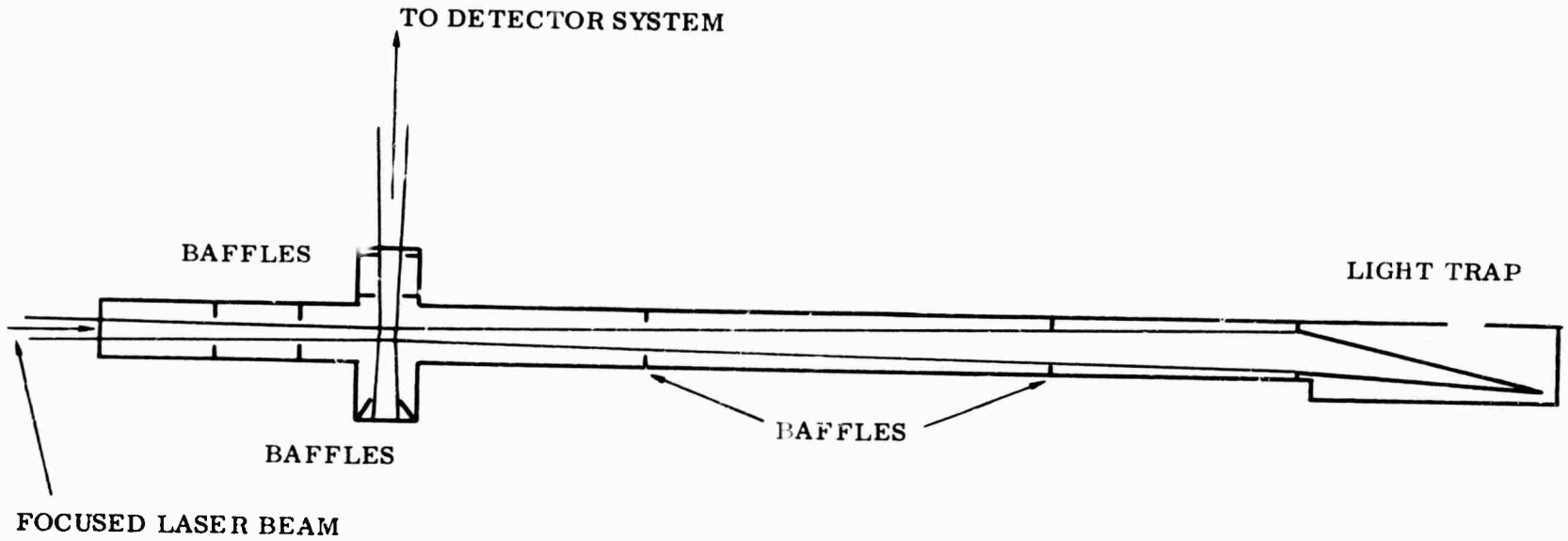

Fig. 12. Scattering Cell with Mylar Baffles and Light Trap.

a. Vacuum. 10 mV/cm, 1.0 μsec/cm

b. 1 atm of CO_2. 10 mV/cm, 1.0 μsec/cm.

Fig. 13. CO_2 Dynamic Calibration

The corresponding result with 1 atmosphere of CO_2 in the cell is shown in Fig. 13b. Measuring the intensity of the signal after the first microsecond and extrapolating back to zero time yields

$$V_{CO_2} = 3 \times 10^{-3} \, p_{CO_2} \, e^{-t/\tau} \quad , \tag{25}$$

where the pressure is given in atmospheres. The measured value of the relaxation time is $\tau = 1.3$ μsec, which corresponds with a rate constant of 3×10^{-15} cm^3/sec, as compared to 9×10^{-15} cm^3/sec reported in the literature.[4] With a noise voltage of 3×10^{-3} volts, this measurement yields

$$\left(\frac{S}{N}\right)_{CO_2} = p_{CO_2} \, e^{-t/\tau} \quad . \tag{26}$$

This signal-to-noise ratio is a factor of two lower than that of Eq. (16). This is the sacrifice required to increase the detector bandwidth to 8 MHz.

The baffle system of Fig. 12, therefore, decreases the wall scattering to approximately 10 times the CO_2 emission. It is expected that this ratio can be decreased further by optimizing the alignment of these baffles and by using a larger scattering cell. At present, we are replacing the three-inch diameter cell with a six-inch system.

Conversion to the larger system will improve the background suppression while leaving the results of Eq. (26) effectively unchanged. Combining Eq. (26) with Eq. (21) then yields

$$\left(\frac{S}{N}\right)_R = \frac{1}{2}\left(\frac{S}{N}\right)_{CO_2}\left(\frac{V_R}{V_{CO_2}}\right) = (0.5 p_{CO_2})(2.4 \times 10^{-10} P_\ell \, p_{N_2})$$

$$= 1.2 \times 10^{-10} P_\ell \, p_{CO_2} \, p_{N_2} \tag{27}$$

for $T_{N_2} = 300^{o}K$ and $p_{CO_2} > 1/3$ atm. The factor of 1/2 in the first line of this equation is required since Eq. (25) was obtained without a filter in front of the IR detector. Consequently, the intensity from both the 9.4μ and 10.4μ bands of CO_2 was measured. For 1 atmosphere of CO_2 and $P_\ell = 4 \times 10^7$ watts/cm^2, the Raman signal-to-noise ratio becomes $4.8 \times 10^{-3} p_{N_2}$. This ratio is clearly insufficient for practical values of the nitrogen pressure. However, increasing P_ℓ to 4×10^8 watts/cm^2 by improved focusing increases this ratio to

$$\left(\frac{S}{N}\right)_R = 4.8 \times 10^{-2} p_{N_2} \quad . \tag{28}$$

Thus, the signal-to-noise ratio for the Raman signal is unity at $p_{N_2} = 20.8$ atm.

These revised figures represent the optimum signal-to-noise ratio attainable for Raman scattering while using the present apparatus. To improve these results requires conversion to the intracavity scattering cell shown in Fig. 2B. Operating within the laser cavity provides a factor of 12.5 increase in the incident laser power. By also inserting a spherical mirror at the bottom of the scattering cell, the scattering signal will be increased by an additional factor of 2. Still another improvement can be obtained with a new Ge:Hg infrared detector. With an antireflection coating on the detector element and the respective detector and load resistances of 50 and 10 KΩ, the signal-to-noise ratio can be increased by a factor of 2. Therefore, by incorporating all these modifications into the present system leads to a signal-to-noise ratio for Raman scattering of

$$\left(\frac{S}{N}\right)_R = (12.5)(2)(2)(4.8 \times 10^{-2} p_{N_2}) = 24 p_{N_2} \quad . \tag{29}$$

By operating a N_2 pressures of 1 to 20 atmospheres, a measurable signal level is provided for the Raman-scattered radiation.

We are presently in the process of converting the experimental apparatus to operate in the intracavity mode while using the six-inch diameter scattering cell. A mirror will be used in the cell. Also, a Ge:Hg detector element, with the features described above, has been purchased and will be inserted into the system.

After installing this new system, the baffles will be aligned to suppress the background sufficiently to allow measuring the Rayleigh scattering from N_2. After this measuring is completed, the absorption cell will be inserted in the optical system. With approximately 0.10 atm of CO_2 in the absorption cell at 600 to 700^{o}K, the Raman scattering from N_2, will be measured.

REFERENCES

1. A. Weber, S. P. S. Porto, L. E. Chessman, and J. J. Barrett, J. Opt. Soc. Amer. 57 19(1967).

2. E. T. Gerry and D. A. Leonard, Appl. Phys. Letters 8 227 (1966).

3. R. L. Taylor and S. Bitterman, "Survey of Vibrational Relaxation Data for Processes Important in the CO_2-N_2 Laser System," Rev. Mod. Phys. 41 26 (1969).

4. W. A. Rosser, Jr., A. D. Wood, and E. T. Gerry, "Deactivation of Vibrationally Excited Carbon Dioxide (ν_3) by Collisions with Carbon Dioxide or with Nitrogen," J. Chem. Phys. 50 11(1969).

APPENDIX

SCATTERING FROM THE WALLS AND FROM DUST

A.1 Wall Scattering

A major requirement in this experiment is to eliminate radiation that scatters from the wall into the detection center. This requirement is particularly important in this experiment because of the small Raman scattering cross section. To illustrate the difficulty, consider the fraction of the laser beam Raman-scattered by the nitrogen at 10 atmospheres pressure and 110°K. The fraction scattered per cm of beam is $\sigma_R [N_2] = 8 \times 10^{-35} \times 10^{21} = 8 \times 10^{-14}$ where σ_R is Raman scattering cross section, and $[N_2]$ is the nitrogen number density. Thus, only one photon in about 10^{13} scatters per steradian. The CO_2 absorption cell in the infrared detection system reduces the scattered radiation by approximately 10^4. (Refer to Figs. 3 and 4.) Thus, less than one photon in 10^9 is the upper limit of the radiation that can scatter off the wall in the direction of the detection system. We have designed a baffle system to investigate if this kind of background suppression can be achieved. Preliminary measurements make us confident that this can be achieved.

The experimental arrangement of the laser beam and the detection system in this scattering chamber is shown in Fig. 5. A lens with a one-meter focal length focuses the laser beam at this scattering region. Measurements of the size of the laser spot at the focal point show a maximum spot diameter of about 4 mm with a sharp boundary. This size spot is consistent with the operation of the laser cacity; the beam in the cavity is about 3 cm across; and the distance between mirrors is the order of 3 meters. This arrangement corresponds to an angular aperture of the beam on the order of three milliradians, which is consistent with beam size measured at the focal point.

To determine the intensity of the beam outside the beamspot, we made the following measurements: (The experimental arrangement is shown in Fig. A1.) An 8-mm diameter mylar disc was placed at the focal point of the

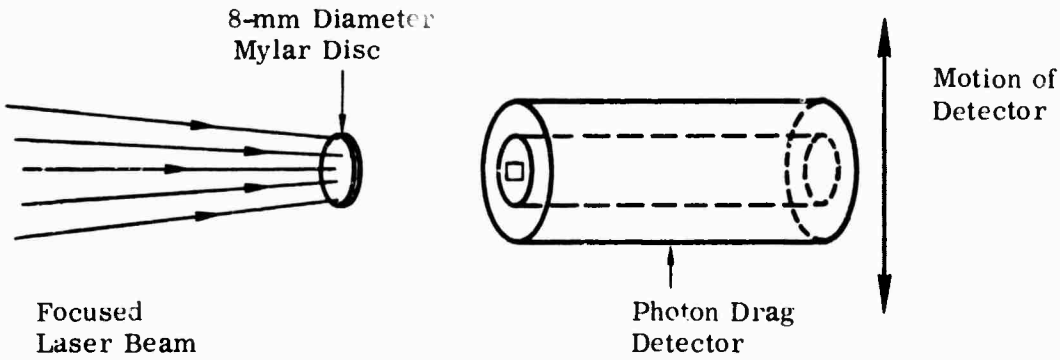

Figure A1. Experimental Arrangement to Determine Laser Intensity Outside Beamspot.

lens. This is the region where the infrared measurements are made. A photon drag detector was used to measure the laser radiation in the region downstream of the disc. The intensity of the laser beam illuminating the mylar disc was 7×10^5 kw/cm^2. The photon drag detector has a sensitivity of 1 kw/cm^2. The drag detector was placed behind the disc and moved radially away from the disc. No observed radiation was detected. This set an upper limit of 1 kw/cm^2 flux behind the plane of the mylar disc. Thus the beam intensity outside the disc diameter was less than 1.4×10^{-6} of the main beam.

The baffle system to remove the stray beam is very simple and only a requirement of the order of 10^4 rejection is required. This rejection is accomplished by placing a baffle, about 8 mm in diameter, 12.5 cm upstream of the focal point. In order to minimize the effects of scattering from this baffle, an additional baffle with a hole of larger diameter is placed 2.5 cm downstream of the main baffle.

The more important background source arises from the beam that passes through the scattering chamber and is incident on the back of the scattering chamber. In order to minimize the backscattering of this radiation into the measurement region, a conical mylar horn is placed in the beam. This horn serves to absorb the beam and to cause multiple reflections into the horn's apex. In addition, the horn is placed about 140 cm from the scattering chamber to reduce the solid angle of the measurements region as seen from the horn. A baffle placed 15 cm downstream of the measurements region defines the amount of beam that can return from the horn. The fraction of the laser beam that can scatter into the measurement region is given by the relation

$$\text{Fraction Backscattered Into Measurement Region} = \left(\frac{A_{disc}}{2\pi f^2}\right)\left(R_{eff}\right) \qquad \text{(A-1)}$$

$$< \frac{\pi(0.6)^2}{2\pi(130)^2}\,(10^{-2}) = 10^{-7} \quad ,$$

where A_D is the area of the downstream aperture; ℓ is the distance from the horn to the diaphragm; and R_{eff} is the effective reflection coefficient back from the horn. We assumed that $R_{eff} = 0.01$. To keep the fraction scattered into the detection system below 10^{-10}, a further suppression of 10^3 is needed. For baffle materials with reflectivities of 5%, three scatterings of the light are required before the light can enter the optical system's field of view. This should be easy to achieve since the light returning from the horn hits the upstream baffle; two further reflections are required by the baffles along the optical system field of view. Thus, we feel that the severe requirement of attenuating any scattered wall light by a factor of 10^{10} is possible. Preliminary measurements of the wall-scattered light indicate that it is about 10^4 times the signal expected for the Raman scattering at high N_2 pressure. The measurements were obtained with no baffles in the chamber and without the CO_2 absorption cell in the path of the optical system. This result is consistent with our estimation of the scattered light.

A.2 Scattering from Dust in Gas

Scattering from dust in the gas could be an important source of radiation if the dust particles are large. However, gas purifying filters are available that remove all particles above 0.1-micron diameter – 1% of the laser wavelength. It is proposed to flow the gas at a low speed through the apparatus and to filter the gas that enters the scattering chamber. The gas filtering will be done by standard Millipore filters. The following pages A5 and A6 are copied from the Millipore catalog and show the variety of filters that are made. We are using the MF Millipore filter (indicated by the arrows) that filters out particles larger than 0.05 ± 0.003 microns in diameter. The filter type used is type VM.

We will now calculate the number of particles of 0.1-micron diameter needed to produce a signal comparable to the signal from the Raman scattering. The fraction of the beam scattered by a particle is given by

Millipore filters are thin porous structures composed of pure and biologically inert cellulose esters or similar polymeric materials. They are currently produced in more than twenty distinct pore sizes, from 14 micrometers to 25 nanometers (0.025 micrometer), in discs ranging from 13 to 293 mm in diameter.

Uniformity of Pore Size

The pores in Millipore filters are extraordinarily uniform in size. For example, the total range of pore size distribution in the Type HA filter (mean pore size 0.45 micrometer) is plus or minus 0.02 micrometer.

High Porosity

Each square centimeter of Millipore filter surface contains millions of capillary pores which occupy approximately 80% of the total filter volume.

High Flow Rate

High porosity and pore configuration result in flow rates through Millipore filters at least 40 times faster than through conventional filters approaching the same particle size-retention capability. Standard flow rate data for water and air are given on page 1A050.

FILTER MATERIAL	PORE SIZE and VARIATION in micrometers (μm)	
Duralon	14	±3
Mitex	10	±2
MF-Millipore	8	±1.4
Duralon	7	±2
Mitex	5	±1.5
MF-Millipore	5	±1.2
MF-Millipore	3	±0.9
Polyvic	2.0	±0.5
Solvinert	1.5	±0.5
MF-Millipore	1.2	±0.3
Duralon	1.0	±0.3
Celotate	1.0	±0.1
MF-Millipore	0.8	±0.05
MF-Millipore	0.65	±0.03
Polyvic	0.6	±0.05
Solvinert	0.5	±0.05
Celotate	0.5	±0.05
MF-Millipore	0.45	±0.02
MF-Millipore	0.3	±0.02
Solvinert	0.25	±0.03
MF-Millipore	0.22	±0.02
Celotate	0.20	±0.05
MF-Millipore	0.10	±0.008
MF-Millipore	0.05	±0.003
MF-Millipore	0.025	±0.003

Fig. 1A1. Millipore filters are produced in a variety of materials (described on page 1A040) and in more than twenty different pore sizes, ranging from 14 micrometers to 25 nanometers.

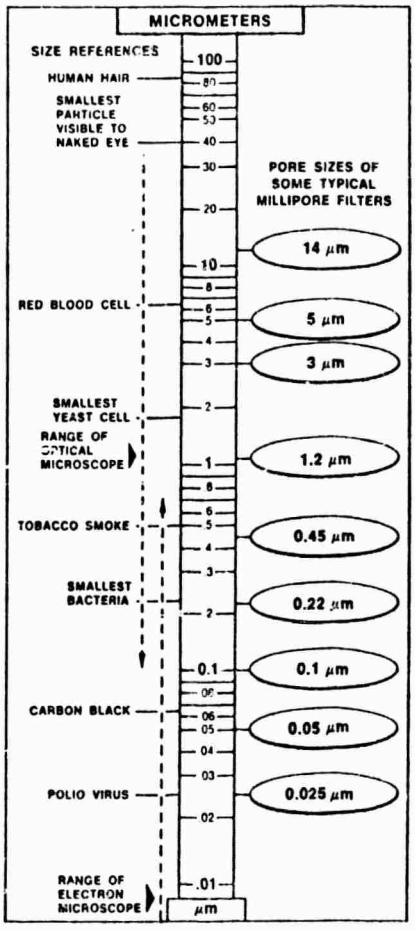

Fig. 1A2. Scale comparing Millipore filter pore sizes with microbes and micro-particles.

Absolute Surface Retention

When fluids are passed through Millipore filters, all particles larger than the pores are retained on the filter surface. This absolute surface retention makes Millipore filters ideal for determining the degree and type of contamination and also for removing trace quantities of solid contaminants from fluids.

Solubility and Chemical Resistance

Millipore filters are made from a variety of polymer materials to provide virtually a complete range of chemical resistance characteristics — even for use in extreme cases with concentrated acids and alkalies. A comprehensive chemical compatibility table for all filter Types will be found on page 6A010, and a brief guide to the proper selection of individual Types on page 1A060.

Filter Specifications

FILTER TYPE	MEAN PORE SIZE	FLOW RATE[1] WATER[2]	AIR[3]	POROSITY (%)	AUTOCLAVABLE[4]	REFRACTIVE INDEX	BUBBLE POINT[5] (psi)
MF-Millipore® (mixed esters of cellulose)							
SC	8.0μm	850	55	74	Yes	1.515	4
SM	5.0μm	540	35	84	Yes	1.495	6
SS	3.0μm	400	20	83	Yes	1.495	10
RA	1.2μm	300	15	82	Yes	1.512	12
AA	0.80μm	212	11	82	Yes	1.510	16
(black)		212	11	82	No	none	16
DA	0.65μm	150	10	81	Yes	1.510	21
HA	0.45μm	52	4	79	Yes	1.510	33
(black)		52	4	79	No	none	33
PH	0.30μm	40	3.7	77	Yes	1.510	40
GS	0.22μm	21	2.5	75	Yes	1.510	55
VC	0.10μm	2	0.49	74	Yes	1.500	250
▶VM	0.05μm	1	0.31	72	Yes	1.500	375◀
VS	0.025μm	0.2	0.22	70	Yes	1.500	500
Duralon® (nylon)							
NC	14.0μm	1020	130	68	No	See	2.5
NS	7.0μm	610	50	65	No	Note	4
NR	1.0μm	270	13	63	No	[6]	12
Solvinert® (solvent resistant — proprietary)							
UR	1.5 m	260[7]	9	79	Yes	n.a.	5[5]
UH	0.5μm	42[7]	3.5	73	Yes	n.a.	10[5]
UG	0.25μm	8[7]	1.5	67	Yes	n.a.	18[5]
Celotate® (cellulose acetate)							
EA	1.0μm	240	11	74	No	1.47	14
EH	0.5μm	67	5	73	No	1.47	28
EG	0.2μm	21	2.5	71	No	1.47	55
Mitex® (Teflon®)							
LC	10.0μm	170	9	68	Yes	n.a.	0.5[5]
LS	5.0μm	70	6	60	Yes	n.a.	0.9[5]
Polyvic® (polyvinyl chloride)							
BS	2.0μm	312[7]	10	79	No	1.528	4[5]
BD	0.6μm	45[7]	4	73	No	1.528	10[5]
Microweb® (nylon-reinforced MF-Millipore)							
WS	3.0μm	155	7.1	45	No	n.a.	12
WH	0.45μm	55	4.5	43	No	n.a.	40

Flow Rate correction for viscosity. For a liquid having a viscosity significantly different from that of water (1 centipoise), divide the flow rate for water by the viscosity of the liquid in centipoises to obtain the approximate initial flow rate. This same correction can also be applied to the flow rates for individual pressure-type filter holders appearing in this Catalog.

45

Notes

(1)Depending upon filter Type, actual flow rates may vary by ±5% to ±33% from the average values given here. Variability is roughly proportional to filter pore size.

(2)Water flow rates are milliliters per minute per cm² of filtration area, at 25°C with a pressure differential of 70 cm of mercury (13.5 psi).

(3)Air flow rates are liters per minute per cm² of filtration area, at 25°C with a pressure differential of 70 cm of mercury (13.5 psi).

(4)See page 1A070 for special Sterile Packed filters. Non-autoclavable Millipore filters may be sterilized with ethylene oxide, by U.V. light, by high-voltage bombardment, or equivalent "cold" methods.

(5)Bubble point, in pounds per square inch, is the pressure required to force air through the pores of a water-wet filter (except: alcohol-wet for Solvinert, Mitex, and Polyvic filters).

(6)Duralon filters cannot be made completely transparent with immersion oil. They become sufficiently translucent with 1.515 N, oil, however, for some transmitted-light microscopy techniques.

(7)Flow rates for Solvinert and Polyvic filters are based on methyl alcohol instead of water.

Thickness of Millipore filters ranges in mean value from approximately 125μm to 150μm according to filter Type, and is controlled to within ±10μm for each Type. See page 1A090 for special ultrathin filters and matched-thickness filters.

Extractables account for between 1.5% and 6% of the weight of the filter, depending upon filter Type.

Tare weight is approximately 5 milligrams per square centimeter for most filter Types, ranging from approximately 3 mg/cm² for MF-Millipore Types SM and SS, to 8 mg/cm² for Mitex filters.

Tensile strength is unusually high, ranging from approximately 150 psi, to over 1,000 psi for MF-Millipore Types VM and VS.

$$\text{Fraction of Beam Scattered} = \frac{\text{Effective Scattering Area of Particle}}{\text{Cross-Sectional Area of Laser Beam}}$$

$$= \frac{\eta(\sigma_{\text{geometric}}/4\pi)}{A_{\text{laser}}}$$

$$= \frac{\left[\frac{8}{3} R P_{\perp} \left(\frac{\pi D_p}{\lambda}\right)^4\right]\left[\frac{\pi}{4}\left(D_p^2/4\pi\right)\right]}{(\pi/4)(D_\ell)^2}$$

$$= 1 \times 10^{-16} R P_{\perp} \quad ,$$

where η = scattering efficiency; $\sigma_{\text{geometric}}$ is the cross-sectional area of the particle; A_{laser} = cross-sectional area of laser beams; D_p = particle diameter = 0.1 microns; D_ℓ = laser beam diameter = 0.4 cm; λ = 10 microns; R = reflectivity of particle; and $P_{\perp}$ is the cross polarization scattering probability at 90° scattering angle. $P_{\perp}$ = 0 for spheres and 0.5 for reflecting dipoles at 45° azimuthal angle. Since about 10^{-9} of the photons are Raman-scattered per steradian, $>10^7$ particles/cm^3 at 0.1μ diameter are required to produce the same scattering into the detector as the Raman scattering. This particle density is orders of magnitude above the expected dust level in the gas. Thus, scattering from dust by 10μ radiation does not seem important.